Translational Oncology
www.transonc.com

Volume 8 Number 6 December 2015 pp. 463–473 463

Quantification of Ultrasonic Scattering Properties of *In Vivo* Tumor Cell Death in Mouse Models of Breast Cancer[1]

Hadi Tadayyon[*,†], Lakshmanan Sannachi[*,†,‡,§], Ali Sadeghi-Naini[*,†,‡,§], Azza Al-Mahrouki[*,‡], William T. Tran[‡], Michael C. Kolios[†,¶] and Gregory J. Czarnota[*,†,‡,§]

*Physical Sciences, Sunnybrook Research Institute, Sunnybrook Health Sciences Centre, Toronto, ON, Canada; [†]Department of Medical Biophysics, Faculty of Medicine, University of Toronto, Toronto, ON, Canada; [‡]Department of Radiation Oncology, Odette Cancer Centre, Sunnybrook Health Sciences Centre, Toronto, ON, Canada; [§]Departments of Radiation Oncology, Faculty of Medicine, University of Toronto, Toronto, ON, Canada; [¶]Department of Physics, Ryerson University, Toronto, ON, Canada

Abstract

INTRODUCTION: Quantitative ultrasound parameters based on form factor models were investigated as potential biomarkers of cell death in breast tumor (MDA-231) xenografts treated with chemotherapy. *METHODS*: Ultrasound backscatter radiofrequency data were acquired from MDA-231 breast cancer tumor–bearing mice ($n = 20$) before and after the administration of chemotherapy drugs at two ultrasound frequencies: 7 MHz and 20 MHz. Radiofrequency spectral analysis involved estimating the backscatter coefficient from regions of interest in the center of the tumor, to which form factor models were fitted, resulting in estimates of average scatterer diameter and average acoustic concentration (AAC). *RESULTS*: The AAC parameter extracted from the spherical Gaussian model was found to be the most effective cell death biomarker (at the lower frequency range, $r^2 = 0.40$). At both frequencies, AAC in the treated tumors increased significantly ($P = .026$ and .035 at low and high frequencies, respectively) 24 hours after treatment compared with control tumors. Furthermore, stepwise multiple linear regression analysis of the low-frequency data revealed that a multiparameter quantitative ultrasound model was strongly correlated to cell death determined histologically posttreatment ($r^2 = 0.74$). *CONCLUSION*: The Gaussian form factor model–based scattering parameters can potentially be used to track the extent of cell death at clinically relevant frequencies (7 MHz). The 20-MHz results agreed with previous findings in which parameters related to the backscatter intensity (i.e., AAC) increased with cell death. The findings suggested that, in addition to the backscatter coefficient parameter AAC, biological features including tumor heterogeneity and initial tumor volume were important factors in the prediction of cell death response.

Translational Oncology (2015) 8, 463–473

Introduction

Locally advanced breast cancer is characterized as a 5-cm or larger tumor often with involvement of the axillary lymph nodes and skin and may include the chest wall. This disease is generally inoperable and requires upfront chemotherapy treatment for local and metastatic control. Despite advancements in chemotherapeutics and the availability of a spectrum of modern drugs including targeted and systemic drugs, positive tumor response does not always occur. This makes the early assessment of tumor response to treatment potentially

Address all correspondence to: Gregory J. Czarnota, Department of Radiation Oncology, Sunnybrook Health Sciences Centre, 2075 Bayview Avenue, T2-167, Toronto, Ontario, M4N 3M5.
E-mail: Gregory.Czarnota@sunnybrook.ca

[1] Funding for this project was also provided by the Terry Fox Foundation, the Natural Sciences and Engineering Research Council of Canada, and the Canadian Institutes of Health Research.
Received 8 October 2015; Revised 30 October 2015; Accepted 2 November 2015

1936-5233/15
http://dx.doi.org/10.1016/j.tranon.2015.11.001

beneficial for refractory patients, as the drug regimen can in principle be changed to a more effective regimen or a different type of treatment. This also has the potential benefit of avoiding adverse side effects and unnecessary costs. Currently accepted methods of response assessment are based on a reduction in the sum of largest diameters of target lesions or the largest diameter of unifocal disease [1]. However, clinically detectable tumor shrinkage does not occur typically until several weeks to months into treatment. In addition, tumor size assessments are only usually made using imaging months after the completion of treatment. In this light, imaging assessments of tumor biology and biochemistry have led recently to the discovery of novel biomarkers that can provide earlier indications of tumor response to therapy [2]. For instance, diffusion-weighted magnetic resonance imaging (MRI) has been demonstrated clinically to predict the response of brain tumors as early as 3 weeks after the initiation of treatment. That method measures changes in the Brownian motion of water in tumor tissue; water diffusion is thought to increase in responding tumors due to a decrease in tumor cellularity [3]. In nuclear imaging, longitudinal positron emission tomography imaging studies on breast cancer have demonstrated a reduced fluorodeoxyglucose uptake in responding tumors after one cycle of chemotherapy [4]. Using a different modality, studies with diffuse optical imaging investigating breast cancer have demonstrated significant changes in hemoglobin concentration, water percentage, and tissue optical index in responding patients as early as 1 week after the start of chemotherapy [5]. The utility of these modalities in the clinic, however, remains limited due to the requirement of contrast agents (MRI), low resolution (diffuse optical imaging), and limits related to the repeated use of radioactive material (positron emission tomography). In contrast, ultrasound offers short image acquisition times, relatively low cost, ionizing-radiation-free imaging, relatively high-resolution images, and label-free imaging (no contrast agents required). For these reasons, ultrasound has received recent widespread attention as a noninvasive therapy monitoring tool in addition to its well-established diagnostic and visualization capabilities.

Quantitative ultrasound (QUS) has been used extensively for various tissue characterization applications, including characterization of normal and pathological breast tissues [6–8], prostate cancer detection [9,10], cancerous lymph node detection [11], and characterization of diffuse liver diseases [12–15]. Such applications use conventional frequency ultrasound which operates generally in the 1- to 10-MHz frequency range where one is less concerned with spatially resolving tissue microstructure and is more interested in the frequency-dependent backscatter properties of different tissues (which are affected by tissue microstructure). High-frequency ultrasound (>20 MHz) offers a higher spatial resolution at the cost of reduced penetration depth (<2 cm). Its uses include scanning acoustic microscopy [16], characterization of inflammatory and neoplastic lesions in excised lymph nodes [17], and detection of cell death *in vivo* [18]. High-frequency QUS has been demonstrated to be a power tool for cell death detection in cancer therapy assessment. The first high-frequency QUS studies of cell death in cancer cells induced by a chemotherapeutic agent demonstrated that apoptosis causes an increase in ultrasound echogenicity [18,19]. These ultrasound changes were later quantified by system-independent parameters including midband-fit (MBF) and spectral slope (SS), both of which demonstrated an increase as a result of cell death [20]. This observation was experimentally determined to be related to the nuclear condensation and fragmentation that occur during apoptosis. The same pattern of changes in ultrasound parameters was observed in animal cancer models *in vivo*, resulting from photodynamic therapy [21] or radiation therapy [22] of mouse tumor xenografts. More recently, a study on the low-frequency (7 MHz) QUS assessment of an animal model of breast cancer treated with chemotherapy demonstrated that increases in the MBF and spectral intercept (SI), but not SS, were strongly correlated to increases in cell death [23]. The MBF, SI, and SS parameters have been used in the past for other tissue characterization purposes, including the detection of prostate cancer, malignancies in lymph nodes, uveal melanoma, and characterizing liver disease [9,11,24,25]. By modeling the ultrasonic power spectrum as a linear approximation of the acoustic impedance autocorrelation, Lizzi et al. demonstrated that the SS is related to the scatterer size, SI is related to scatterer size and acoustic concentration, and MBF is related to the scatterer size, acoustic concentration, and attenuation [26]. Furthermore, the fitting of advanced form factor models to ultrasonic tissue backscatter has recently permitted the direct estimation of scattering properties of tissues, including average scatterer diameter (ASD) and average acoustic concentration (AAC). A form factor is proportional to the Fourier transform of the spatial autocorrelation of the relative acoustic impedance between the scatterer and the background. The AAC parameter is a product of the average number of scatterers per unit volume and mean square variation in acoustic impedance of the scatterer and background [27]. These parameters have been demonstrated to be useful in differentiating between tumor types *in vivo*, including sarcoma, carcinoma [28], and fibroadenoma [29]. More recently, a clinical QUS study demonstrated significant increases in AAC in breast tumors of patients who responded well to chemotherapy treatment, compared with those who did not respond well, as early as 1 week after the start of treatment [30].

Various form factor models have been developed to describe tissue scattering, including the spherical Gaussian model (SGM) and the fluid-filled sphere model (FFSM) [31]. The SGM describes random scattering and a continuous variation of acoustic impedance between the scatterer and its surrounding, and has an impedance autocorrelation which follows a Gaussian function. In contrast, the FFSM describes scattering by randomly distributed fluid-filled spheres, in which the cell nuclei are considered scatterers and the cytoplasm and the extracellular material are assumed to be background material. Good fits have been observed with both models depending from which kind of tissue ultrasound data were obtained. Regardless, extensive evidence demonstrates that nuclear material contributes to backscattered ultrasound signals. There are multiple sources of experimental evidence suggesting the role of nuclear structure in potentially influencing significantly ultrasound backscatter signals. This evidence spans work *in vitro*, cellular experiments with cellular structure–modifying agents, investigations of different cell types with different nuclear sizes, and work with isolated nuclei from viable and apoptotic nuclei [18,32,33].

To date, very few studies have been reported on cell death detection using low-frequency ultrasound (<10 MHz) [23,34]. In addition, linear regression spectral analysis implemented in those studies provides indirect estimates of tissue scattering properties (i.e., ASD and AAC) using a simplified model. In this study, we used an advanced QUS analysis technique in which scattering models including the SGM and FFSM were fitted to backscatter coefficient (BSC) estimates computed from radiofrequency (RF) data from

xenograft tumors undergoing cell death to obtain direct estimates of scattering properties. First, we compared the two scattering models in terms of their goodness of fit with measurements, and agreement of scatterer size estimates with histology. Second, we tracked their time-dependent cell death responses using the better model determined in the first step and compared their correlation to histologically determined cell death extent. Statistical tests were performed to compare changes in ASD and AAC related to treatment against those related to tumor progression (control), including analysis of variance (ANOVA) and *post hoc* tests. Multiple regression analyses were performed on changes in ultrasonic scattering properties and the extent of cell death observed histologically.

Methods

Experimental Procedures

The experimental protocol was approved by the institution's animal care committee for the humane and ethical use of laboratory animals. Human breast cancer cell line tumors (MDA-MB231, American Type Culture Collection, Manassas, Virginia) were established by injection of 1×10^6 cells in 50 μl of PBS into the hind legs of severe combined immunodeficiency disease mice and were permitted to grow to ~1-cm solid tumors. During treatment and imaging, mice were anesthetized with 100 mg/kg of ketamine, 5 mg/kg of xylazine, and 1 mg/kg of acepromazine (CDMV, St. Hyacinthe Quebec, Canada). The chemotherapeutic agents paclitaxel and doxorubicin (100 mg/m^2 and 50 mg/m^2, respectively) were injected intravenously through the tail. Pulse-echo imaging was performed before injection and at a predetermined amount of time after injection. Experimentation used 20 animals equally divided into 5 groups ($n = 4$). The first 4 groups were the treatment groups with 4, 12, 24, and 48 hours of wait time after chemotherapy injection, respectively, and the fifth group served as untreated control tumors (0 hour).

Low- and high-frequency ultrasound data were acquired using two imaging systems: a Sonix RP system (Sonix RP, Ultrasonix, Vancouver, Canada) operating a 7-MHz linear array transducer (L14-5/38) focused at 1.5-cm depth, with data sampled at 40 MHz, and the Vevo 770 system (Visual Sonics, Toronto, Canada) employing a 20-MHz transducer (RMV-710B) focused at 9-mm depth, with data sampled at 420 MHz. Both systems were used to collect volumetric data with scan plane separations of ~0.5 mm in the low-frequency ultrasound and ~0.1 mm in the high-frequency ultrasound depending on the size of the tumor. Tumor volumes were estimated by approximating the tumor volume as an ellipsoid and measuring the three axes (2a, 2b, and 2c) from *in vivo* three-dimensional B-mode images obtained using the high-frequency ultrasound system, and using the formula $\frac{4}{3}\pi abc$ to estimate the volume. The images obtained from the high-frequency system were used for anatomical measurements because that system provided high-resolution tumor images and more accurate tumor delineation.

Histology Analysis

Histology analysis was performed on excised tumor sections which were fixed in 5% formalin (volume/volume) in PBS. Each fixed specimen was sectioned into five slices stained for hematoxylin and eosin (H&E) and five slices stained for *in situ* end labeling (ISEL), with 50-μm spacing. The cell death fraction (CDF) of each tumor was determined using ImageJ (National Institutes of Health, Bethesda, MD) by manually contouring the ISEL-positive (brown stain) area and the total tumor area and taking the ratio of the two areas. The mean CDF for each tumor was obtained by averaging the CDFs from all five tumor sections. High-magnification images were obtained using a Leica DC100 microscope with a 40× objective and a Leica DC100 camera connected to a 2-GHz PC running Leica IM1000 software (Leica GmbH, Wetzlar, Germany). Areas which were identified as ISEL positive for CDF calculation were verified under high magnification to contain more than 50% apoptotic cells. Mean cell and nucleus sizes were estimated by manually measuring the diameters of approximately 100 cells and corresponding nuclei in the ISEL-stained sections under high magnification.

QUS Analysis

For analyses, rectangular regions of interest (ROIs) were selected from 5 to 10 tumor cross-section data sets. These ROIs accounted for approximately 2/3 of the tumor cross sectional area in ultrasound images (approximately 5-10 × 5-10 mm in-plane and 5-10 mm through plane). A sliding window analysis was performed on each ROI using Hanning-gated RF windows of 2 × 2–mm size for low-frequency data and 0.62 × 0.62–mm size for high-frequency data, with 80% overlap between adjacent windows in both axial and lateral directions. The axial length of the RF segments was selected to cover approximately 10 wavelengths, which corresponded to the minimum size required to obtain reliable spectral estimates which were independent of window length (10 wavelengths) [35]. Each window spanned 13 RF scan lines in the low-frequency images and 11 RF scan lines in high-frequency images, respectively. The theoretical BSC was defined as follows [31]:

$$\sigma_b(k) = \frac{\overline{n}\gamma^2}{9} k^4 a^6 F(k, a) \tag{1a}$$

$$\gamma^2 \cong 4\left(\frac{Z_{\text{scatterer}} - Z_{\text{background}}}{Z_{\text{background}}}\right)^2, \tag{1b}$$

where $F(k, a)$ is the form factor, $\overline{n}$ is average number of scatterers per unit volume, Z is acoustic impedance, and $\overline{n}\gamma^2$ is the AAC, $k = \frac{2\pi f}{c}$ is the wave number, and a is the scatterer radius. The measured BSC was computed by applying the reference phantom technique to the attenuation compensated normalized power spectrum, as follows [36]:

$$\hat{\sigma}_b = \frac{S_s(f)}{S_r(f)} e^{4(\alpha_s - \alpha_r)\left(R + \frac{\Delta z}{2}\right)} \hat{\sigma}_{br}, \tag{2}$$

where $S_s(f)$ is the mean sample power spectrum, $S_r(f)$ is the mean reference power spectrum, α_s and α_r are the sample and reference attenuation functions, R is the distance from the transducer surface to the proximal edge of the RF window, Δz is the gate length, and $\hat{\sigma}_{br}$ is the reference BSC. The mean power spectrum, $S_s(f)$, of each RF window was computed by taking the squared magnitude of the fast Fourier transform of the Hanning-gated RF signal from every scan line and averaging the result across the scan lines. Spectral calibration [dividing $S_s(f)$ by $S_r(f)$] was carried out to remove system-dependent effects such as transducer transfer function and beam forming. The reference material used for spectral calibrations was a phantom consisting of glass microspheres (5-40 μm)

embedded in agar gel and modified from Ref. [37]. The reference BSC, $\hat{\sigma}_{br}$, was obtained using pulse-echo technique and planar reflector (Plexiglas) calibration as described in Ref. [27]. The attenuation coefficient of the phantom, α_r, was 0.15 dB/cm-MHz, which was determined through an insertion-loss experiment and fitting a straight line through the attenuation versus frequency data over the two system bandwidths (3-9 MHz and 10-25 MHz) [6]. The normalized power spectrum was then compensated for frequency-dependent attenuation using the point-by-point compensation method [31], assuming published attenuation coefficients, α_s, of 2 dB/cm/MHz and 0.6 dB/cm/MHz for skin [38] and tumor [22], respectively. Scattering properties, including ASD and AAC, were estimated by the minimum of average squared deviation (MASD) fitting of the theoretical BSC (σ_b) and the measured BSC ($\hat{\sigma}_b$) as follows [31]:

$$\text{MASD} = \min\left(\frac{1}{m}\sum_{i=1}^{m} X_i - \overline{X}\right), \tag{3a}$$

where

$$X_i = \log\left(\frac{\hat{\sigma}_b(f_i)}{\sigma_b(a, f_i)}\right) \tag{3b}$$

and

$$\overline{X} = \frac{1}{N}\sum_{i=1}^{N} X_i \tag{3c}$$

This permitted us to generate parametric images of ASD and AAC over the tumor ROI to assess tumor heterogeneity. Two features were extracted from the ASD and AAC maps: the mean and standard deviation [or heterogeneity index (HI)]. We then performed correlation analysis between histologically determined CDF and the changes in the means of ASD and AAC images (ΔASD and ΔAAC) and changes in the HI (standard deviation) of ASD and AAC images (ΔHI_{ASD} and ΔHI_{AAC}) before and after treatment administration. The mean coefficient of determination, $<R^2>$, and sum of squared residuals, $<\chi^2>$, two metrics which indicate the goodness of fit between measured and a theoretically derived backscatter coefficient, were also calculated bearing in mind that these would be affected by tumor heterogeneity. Finally, QUS parametric images were constructed by superimposing color-coded pixels that were mapped to QUS parameter estimate values and locations associated with the sliding window locations on the original gray-scale B-mode image of the tumor [27]. An HI of ASD and AAC that expresses variability of these parameters over the tumor area (standard deviation of the parametric image) was calculated as per Nam et al. [39] to reflect tumor heterogeneity.

Statistical Analysis

In order to evaluate of the goodness of fit of each form factor model, the mean coefficient of determination, $<R^2>$, was computed from all untreated tumors. Levels of CDF and changes in levels of AAC were compared among treatment times using a one-way ANOVA test. This was followed by a *post hoc* test using Fisher's least significant difference (LSD) method to test for statistical significance in each group relative to the control group. A P value less than .05 was considered to be statistically significant. The correlations between CDF and BSC parameters of all tumor samples (N = 17; 3 of the 20 animals died midway in the study) were evaluated using multiple linear regression analysis. All samples were included independent of group affiliation to have enough samples to obtain a meaningful correlation. The Pearson product-moment correlation coefficient, r^2 metric, was used to evaluate the strength of the correlation. The HI was used to highlight the inherent tumor heterogeneity in terms of cell death response and baseline heterogeneity. For analysis of correlation between QUS and histology (CDF), two scenarios were considered: multiple regression analysis on the set (ΔAAC, ΔASD, ΔHI_{AAC}, ΔHI_{ASD}) and multiple regression analysis on the set (ΔAAC, ΔASD, ΔHI_{AAC}, ΔHI_{ASD}, V_i). The second scenario examined the effect of initial tumor volume on the BSC parameters because it is known that tumor size can have effects on tumor microstructure and hence on the prediction of cell death response.

Results

Histological Assessment of Treatment Effects

Figure 1 presents H&E- and ISEL-stained sections of representative control and treatment time groups. Whereas control tumors were characterized by multiple distinct nucleoli-containing cells and microvessels, treated tumors were characterized by loss of microvessels, a decrease in the number of cells with distinct nucleoli, and an increase in the number of cells with condensed nuclei in H&E sections. Treated tumors also demonstrated a heterogeneous increase in the area of brown staining in the extracellular space in ISEL sections. The strong focal stains in the H&E and blue-brown focal stains in the ISEL sections were consistent in appearance with the nuclear condensation stage of apoptosis. The brown staining in the extracellular space in the ISEL was consistent with the appearance of fragmented DNA and cellular debris associated with late stages of apoptosis. Both H&E and ISEL sections indicated that, as time progresses from 0 to 24 hours after the onset of chemotherapy, tumors changed from a heterogeneous mixture of dead and viable cells to an almost homogeneous tissue of dead cells. At 48 hours, tumors appeared to have entered the final stages of cell death marked by nuclear degradation, as evident from a loss of cells with visible nuclei. The mean changes in cell and nucleus size with treatment time are presented in Figure 1*E*. In general, reductions in cell and nucleus size were observed resulting from chemotherapy-induced cell death as time progressed, apparently plateauing at 48 hours. Plots of mean cell death fraction versus treatment condition are presented in Figure 1*F*. Analysis of cell death obtained from ISEL-stained histology images revealed a monotonic increase in cell death with time from treatment onset, peaking at 24 hours, after which the cell death content dropped but remained higher than cell death observed in controls.

Tumor Volume Analysis

Plots of mean tumor volume pre- and posttreatment measured by ultrasound for each experimental condition are presented in Figure 2. The volumes were estimated based on an ellipsoid model using B-mode images obtained from the high-frequency system. Additionally, the percent variability in initial tumor volumes was computed as follows: 74%, 27%, 40%, 20%, and 67% for control, 4-hour, 12-hour, 24-hour, and 48-hour groups, respectively. Percent variability of the mean initial volume was defined as the standard deviation of the initial tumor volume across animals divided by mean initial tumor volume divided by square root of the number of animals in that group. Initial tumor volumes had large variations (varied as

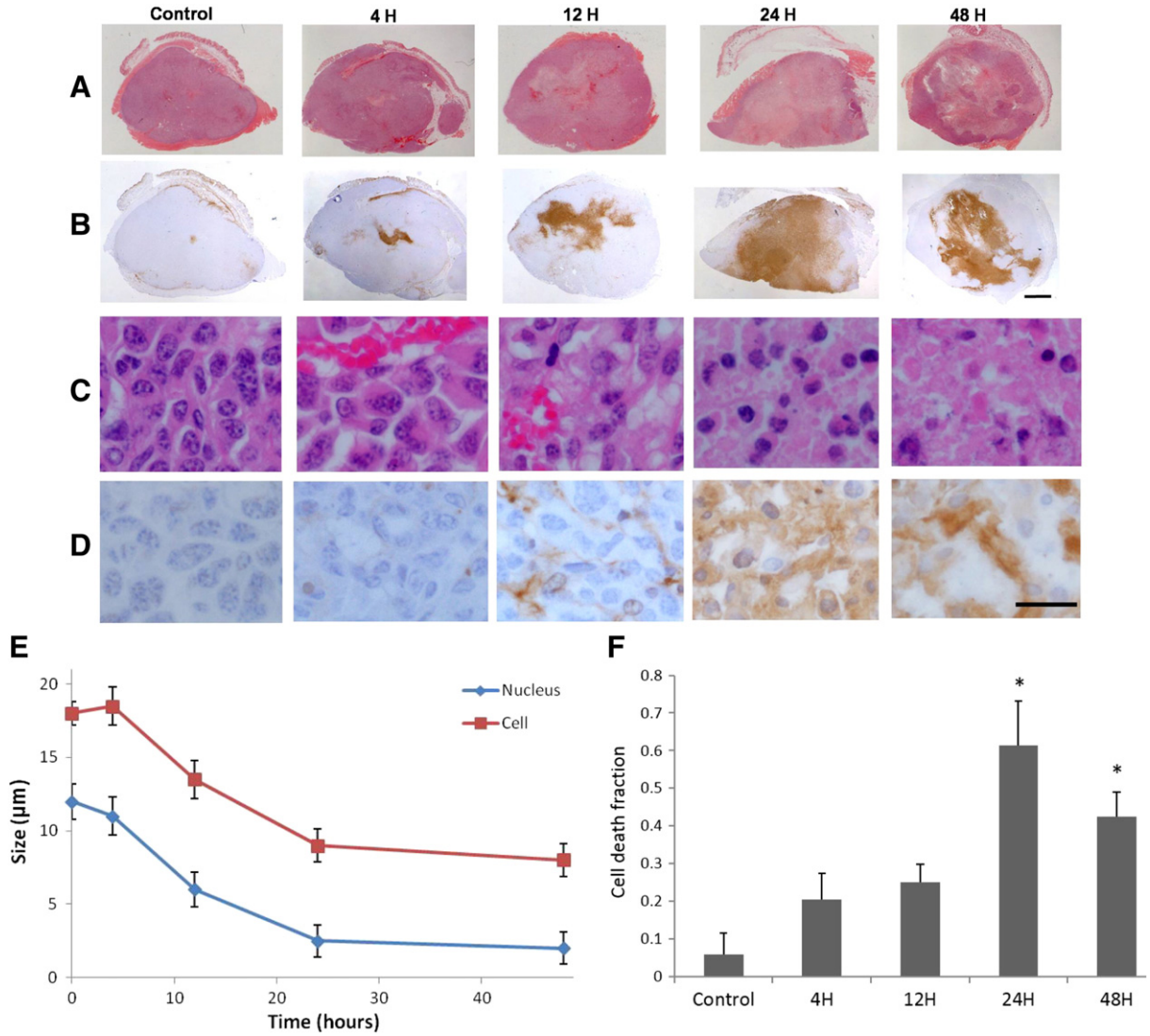

Figure 1. (A-D) Histology images of representative control (0-hour), 4-hour, 12-hour, 24-hour, and 48-hour chemotherapy-treated MDA-231 tumors, from left to right, respectively. (A) Low-magnification H&E-stained sections. (B) Low-magnification ISEL-stained sections. (C) High-magnification H&E-stained section to highlight nuclear material. (D) High-magnification ISEL section to highlight fragmented DNA. The control tumor features rapidly dividing cells with large nuclei. The treated tumors feature reduced nuclear size (nuclear condensation), fragmented nuclei, and dead cellular components filling the extracellular space (brown stains). The low-magnification scale bar represents 1 mm. The high-magnification scale bar represents 25 μm. (E) Plots of mean cell and nucleus diameters versus treatment time (0 to 48 hours) estimated from H& E histology sections. Error bars represent standard error of the mean. (F) Plot of the mean cell death fractions versus time. Error bars represent the standard error across the tumor samples for each time condition. Statistical significance: *$P < .05$.

much as 74%). In both cases of treatment and control, tumor volume increased slightly in time; however, comparison of pre- and posttreatment volumes performed through paired t test for each condition revealed no statistically significant differences ($P > .05$).

Tissue Microstructure Models

Tumor microstructure was examined microscopically in H&E- and ISEL-stained sections to identify and characterize structures that could help understand models of ultrasonic scattering. Figure 1, column 1, presents H&E and ISEL sections of a representative control tumor in low-magnification and high-magnification views. In the H&E sections, tumors appeared to be predominantly composed of tumor cells (purple-stained nuclei), with infrequent microvessels (red-pink stained) and connective tissue (cyan-pink stained). Microvessels were only sparsely observed and had a size of 20 ± 2 µm in cross section. The tumor cells dominated the tumor tissue. Both the H&E and ISEL sections show densely packed cells with high mitotic indices and large nuclei (18 ± 3–µm diameter) containing visible nucleoli.

Table 1 lists the average cell size (histology), ASD, AAC, and mean R^2 ($<R^2>$) goodness of fit, as well as mean sum of squared residuals ($<\chi^2>$) obtained from all pretreated tumor BSC at low and high frequencies using both models. Pretreatment data were used because they permit the characterization of MDA tumors in terms of scattering properties without the necessity to consider complex tissue microstructures which can result from cell death. At the lower frequency range, both models yielded large ASD values (109 ± 12 µm for SGM, 95 ± 9 µm for FFSM, $P < .05$). However, the SGM

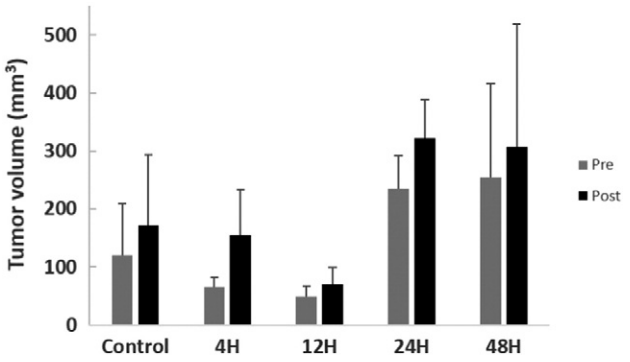

Figure 2. Plot of *in vivo* tumor volumes before (pre) and at predefined length of time after chemotherapy injection (post). Percent variability of the initial tumor volumes for each group was 74%, 27%, 40%, 20%, and 67%, for control, 4-hour, 12-hour, 24-hour, and 48-hour groups, respectively.

provided a better fit to the measured backscatter data ($<R^2>$ = 0.21, $<\chi^2> = 1.98 \times 10^{-5}$) compared with the FFSM ($<R^2>$ = 0.07, $<\chi^2> = 8.07 \times 10^{-4}$). For this reason, the SGM was used going forward, and multiple linear regression analysis was performed using ASD and AAC features extracted from this model. For the high-frequency data, both models provided smaller ASD estimates (45 ± 7 μm for SGM and 38 ± 1 for the FFSM), and the FFSM yielded a statistically significantly smaller ASD compared with the SGM ($P > .05$). Both models yielded similar fits ($<R^2>$ = 0.08 and 0.06 and $<\chi^2> = 5.24 \times 10^{-7}$ and 5.42×10^{-7} for SGM and FFSM, respectively). However, to be able to make comparisons between the two imaging systems, the SGM model was also used for the high-frequency data going forward with CDF correlation analysis. Figure 3 presents combined low- and high-frequency plots of measured BSC and corresponding theoretical BSCs based on the SGM and FFSM models obtained from one of the treated tumors. The BSCs were obtained from an RF window at the center of the tumor ROI at low and high frequencies. Results are shown before and 24 hours after chemotherapy injection. R^2 values ranged from 0.55 to 0.71. The FFSM model provided a better fit at high frequency at pretreatment, whereas no considerable model differences were observed posttreatment. These values were higher compared with the values reported in Table 1 because Table 1 reports the mean of mean R^2 where R^2 was averaged across all windows in the tumor ROI which was subsequently averaged over all pretreatment tumors. However, the R^2 reported in Figure 3 was obtained from one RF window from one animal. Generally, we observed lower R^2 values in more heterogeneous tumors which were linked to tumor size. An increase in the BSC magnitude can be observed from pretreatment to posttreatment at both frequency ranges. This trend was consistent with the trend observed in AAC, which is demonstrated in the next section.

Table 1. Comparison of ASDs and AACs Estimated Using the SGM and FFSM Models at Low and High Frequencies (LF and HF) with Mean Histological Measurement of Tumor Cell Size

Cell Diameter (μm)	18 ± 3							
	SGM				FFSM			
	ASD	AAC	R^2	χ^2	ASD	AAC	R^2	χ^2
7 MHz	109 ± 12	5 ± 9	0.21	1.98×10^{-5}	95 ± 9	7.35 ± 9	0.07	8.07×10^{-4}
20 MHz	45 ± 7	32 ± 19	0.08	5.24×10^{-7}	38 ± 1	−11 ± 11	0.06	5.42×10^{-7}

R^2 (coefficient of determination) and χ^2 (sum of squared residuals) are measures of the goodness of fit of the model BSCs to the measured BSCs. The symbol "±" represents standard deviations of the parameter over the tumor samples. Estimates were obtained from all tumors (N = 17) before treatment. Units: ASD = μm, AAC = dB/cm^3, R^2 = unitless, χ^2 = Sr^{-1}cm^{-1}.

Ultrasonic Scattering Properties of Cell Death

Figure 4 presents AAC and ASD images obtained using the SGM from high- and low-frequency ultrasound imaging, respectively. The corresponding ISEL section posttreatment is also presented. The cytotoxic effects of the treatment could be readily visualized (Figure 4*C*), demonstrating predominantly brown-stained areas indicative of cell death. The AAC images demonstrated that AAC increased considerably as a result of cell death (statistically significant) at both frequencies, whereas the ASD was less sensitive to cell death at both frequencies.

ANOVA test revealed that the mean CDF levels were statistically significantly different among all treatment groups (P = .006), as demonstrated in Table 2. CDF increased statistically significantly at 24 and 48 hours compared with the control group (*post hoc* test $P <$ .05, Table 2). Figure 5 presents mean changes in AAC corresponding to different treatment conditions (control and 4, 12, 24, and 48 hours) obtained from low- and high-frequency RF data. Results demonstrated a parallel trend in the AAC changes with treatment conditions as did the CDF in Figure 1*F*. Initial observations suggested that AAC nominally increased proportionally with time, peaking at 24 hours, following the observations for CDF. However, ANOVA test revealed no statistically significant difference between the means of the five groups at low and high frequencies, although *post hoc* LSD test revealed significant differences between 24-hour and control groups at low (P = .026) and high (P = .035) frequencies, as indicated in Table 2. Other tests were used to assess factors as per below where there were differences.

A stepwise multiple linear regression analysis of CDF versus BSC parameters (ΔAAC, ΔHI_{AAC}, ΔASD, ΔHI_{ASD}) revealed the single most correlated parameter to be ΔAAC with a correlation (r^2) of 0.399. The best multiparameter QUS model was a linear combination of ΔAAC and ΔHI_{ASD} with a correlation of 0.639. Furthermore, when initial tumor volume (V_i) was added to the model on the working hypothesis that gross biological changes in tumor structure associated with tumor growth and size (such as baseline tumor necrosis and vascular content) may affect data, the correlation further increased to 0.744 (Table 3A). Stepwise multiple linear regression analysis of CDF versus tumor volume-normalized BSC parameters (i.e., BSC parameter × V_i) determined the best predictor model to be ΔAAC_{VN} with r^2 = 0.688 (VN stands for volume normalized). An immediate observation was a considerable increase in r^2 attributed to the normalization of ΔAAC to initial tumor volume (i.e., from 0.399 to 0.688). Normalization by division of each BSC parameter by V_i resulted in poorer correlation (r^2 = 0.013). Table 3B lists the model parameters, their standardized coefficients, and their individual correlations to CDF for case 1, when V_i was included in the correlation analysis, and case 2, when all BSC parameters were normalized to V_i before correlation analysis. In case 1, ΔAAC had the strongest correlation (r^2 = 0.399), followed by V_i (r^2 = 0.197) and then by ΔHI_{ASD} (r^2 = 0.068). In case 2, ΔAAC_{VN} had the strongest correlation (r^2 = 0.688), and addition of more parameters did not improve the correlation. Figure 6 presents scatter plots of CDF versus model predictions with lines of least squares fit. Figure 6*A* presents the prediction obtained using the (ΔAAC, ΔHI_{ASD}) model, whereas

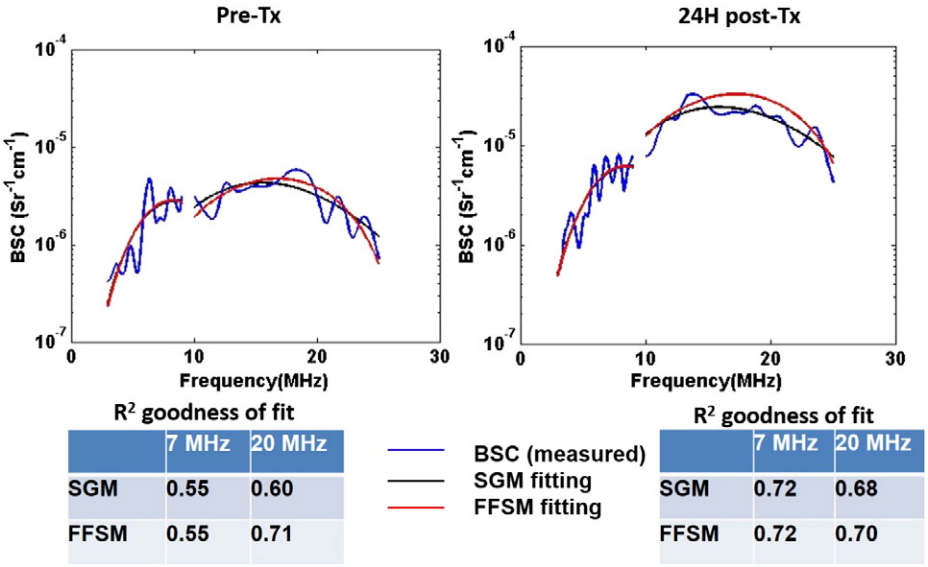

Figure 3. Combined low -and high-frequency plots of measured BSC and theoretical BSCs based on the SGM and FFSM models obtained from an animal in the 24-hour treatment group. Left: pretreatment. Right: posttreatment. The BSCs were obtained from an RF window at the center of the tumor ROI. Corresponding R^2 goodness-of-fit values are shown below the plots.

Figure 6*B* presents the prediction obtained using the (ΔAAC, ΔHI_{ASD}, V_i) model, which was found to be the optimal QUS model.

Discussions and Conclusions

Ultrasound is widely preferred over currently available breast imaging modalities due to its relatively low cost, high spatial and temporal resolution, safety, and independence from external contrast agents. This study demonstrated that scattering properties can be potentially used as biomarkers of treatment response–related cancer cell death at high (20 MHz) and low (7 MHz) ultrasound frequencies. Examination of tumor histopathology revealed clusters of tumor cells and microvessels as dominant features which could serve as potential scatterers of ultrasound with sizes of 18 ± 3 μm and 20 ± 2 μm, respectively. Two scattering properties, ASD and AAC, were estimated using the SGM and FFSM models to provide insight into changes in potential scatterer size and scatterer concentration. Analysis of ISEL-stained histopathology revealed a progressive increase in cell death extent with time up to 24 hours from treatment initiation, after which cell death decreased due to nuclear and cellular degradation (48 hours). Changes in AAC related to cell death were consistent with changes in surrogate measures of AAC (i.e., MBF and SI) that were assessed in previous work [22,23] and changes in backscatter intensity observed in previous *in vitro* studies [19,20]. In the study here, the use of a wider analysis bandwidth permitted a better characterization of the frequency-dependent backscatter of treated and untreated tumors by fitting advanced scattering models as opposed to applying a simple linear regression to the power spectrum within a narrow bandwidth.

Our working model of the ultrasonic scattering properties related to cell death is that nuclear changes are predominantly responsible for the increase in AAC. Because AAC is the coefficient of the BSC, it is related to the backscatter amplitude. Previous *in vitro* and *in vivo* studies suggest that changes in the magnitude and frequency dependence of ultrasound backscatter with cell death arise from coincident changes in the nuclear structure of the cell [18,21,32].

As tumor structure becomes more complex in association with tumor growth, there are further complexities which can be linked to potential sources of ultrasound backscatter. The degree of fit between the SGM and FFSM models and the measured BSC at both low and high frequency ranges were consistent with the work of others (R^2 = 0.1-0.3) [28]. The poor fits were due to tumor heterogeneity and small RF window size used. To examine the effect of window size on BSC fit, a 4-mm window size was examined in addition to the 2-mm window used in this study. In a randomly selected pretreatment tumor, it was found that using a 4-mm window resulted in better model fits than using a 2-mm window (R^2_{SGM} and R^2_{FFSM} were 0.33 and 0.29 for a 4-mm window compared with − 0.04 and − 0.29 for a 2-mm window, respectively). However, using a 4-mm window would result in the inability to visualize tumor heterogeneity (no parametric maps of ASD or AAC), and some small tumors would not accommodate this window size. Thus, 2 mm was chosen because it was the largest window size which permits the characterization of tumor heterogeneity and can accommodate tumors of all sizes in the study. These previous studies have also demonstrated that the degree of model fit to the measured backscatter does not reflect the accuracy of the scatterer size estimates (i.e., agreement between scatterer size and observed microstructure) and models which fit the measurement with less than 0.50 $<R^2>$ can nevertheless estimate the scatterer properties reasonably well [28].

The scattering models that were applied in this study were not used to characterize scattering by individual cells; rather, it is hypothesized that clusters of predominantly tumor cells with a potential contribution from microvessels were detected as scatterers. Immunohistochemical examination of tumors 24 hours after therapy exposure revealed positive staining for cell death covering nearly 60% of the tumor cross-sectional area. Recall that AAC is related to the product of scatterer number density and relative acoustic impedance. Thus, the observed increases in AAC due to cell death may have been also caused by changes in the acoustic impedance of the scatterers relative to the background because nuclear fragments were prominent

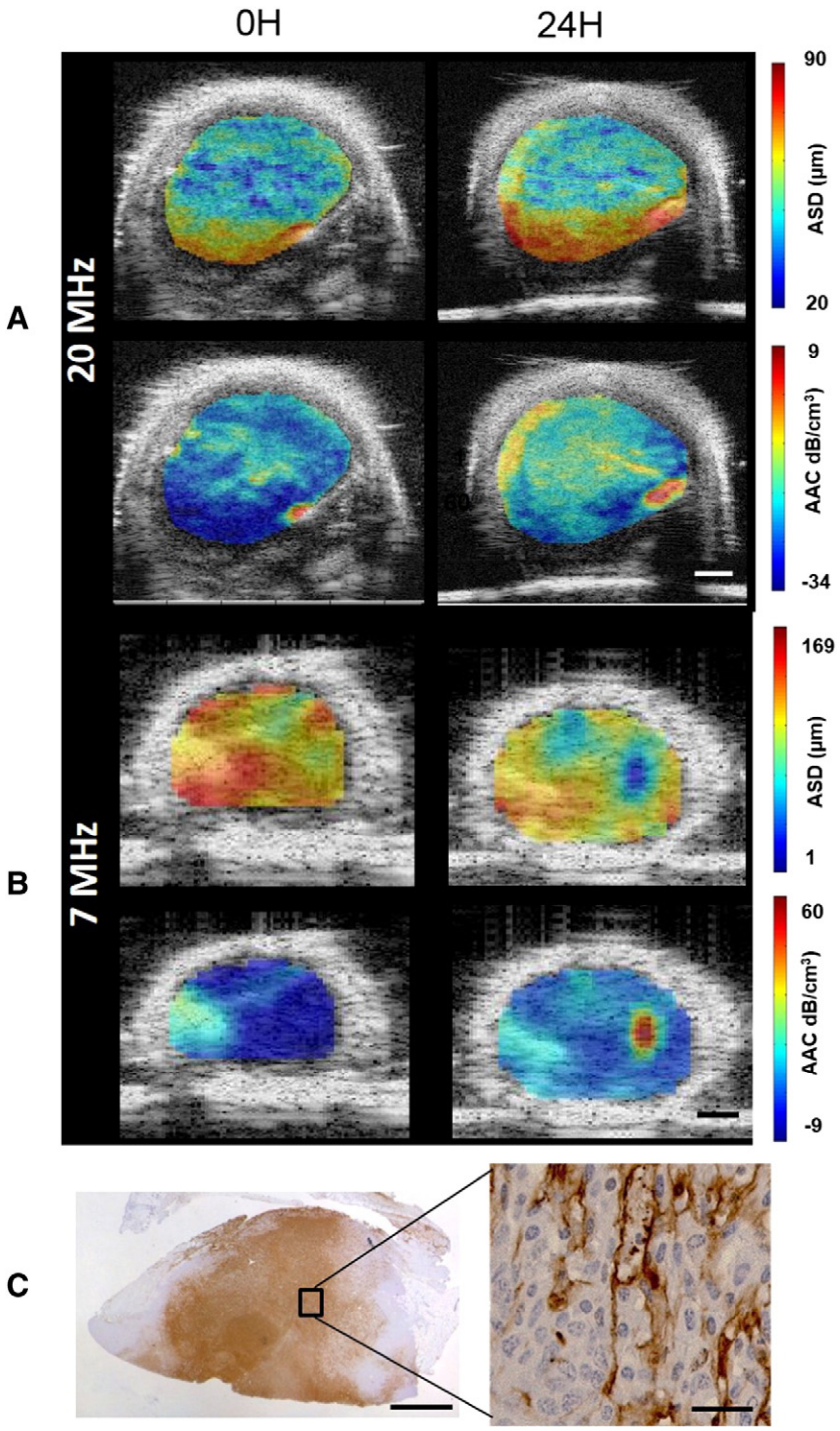

Figure 4. Pre- and posttreatment (24-hour) images of the central cross section of a sample MDA-231 tumor which received chemotherapy treatment. (A and B) High- and low-frequency AAC and ASD images overlaid on the B-mode images, respectively; (C) low- and high-magnification ISEL-stained histology sections of the tumor. B-mode and low-magnification scale bars represents 2 mm. High-magnification scale bar represents 25 μm.

inside dying cells and cellular debris filled the extracellular space. For this reason potentially, AAC showed a stronger correlation to cell death (R^2_{SGM}= 0.40) compared with ASD (R^2_{SGM} = 0.00).

An important finding in this study was that initial tumor volume measurements demonstrated large variations (as high as 74 % of the mean value). This variation was likely due to differences in tumor growth and may explain the weak correlation of AAC as a parameter alone with cell death across tumor samples. As tumors grow beyond 7 to 10 mm, in our experience, more vascularization occurs and also higher baseline levels of necrosis are thought to arise from transient hypoxia. In the study here, we hence included tumor volume as a predictive parameter in the QUS model used. Clinical studies have also used such factors given the complexity of tumor biology linked to tumor size and the effect of this on response. For example, a breast MRI study demonstrated that initial tumor volume is significantly predictive of chemotherapy response of breast cancer patients [40,41].

Table 2. Statistical Significance Tests Comparing the Means of All Treatment and Control Groups Using the ANOVA Test, and Fisher's LSD Test Comparing Each Treatment Group to the Control Group

Parameter	ANOVA Test	*Post Hoc* Test			
		Control vs 4 h	Control vs 12 h	Control vs 24 h	Control vs 48 h
CDF	0.006	0.33	0.14	0.001	0.038
AAC (LF)	0.339	0.179	0.128	0.026	0.140
AAC (HF)	0.425	0.101	0.102	0.035	0.068

Results are presented for CDF, ΔAAC (LF), and ΔAAC (HF).
$P < .05$.

Table 3A. Stepwise Multiple Regression Results

Predictive model	Correlation to CDF
ΔAAC	0.399
ΔAAC, **Δ**HI_{ASD}	0.639
ΔAAC, **Δ**HI_{ASD}, V_i	0.744

The second column presents the standardized coefficient of each model, and the third column presents the model's correlation to CDF (r^2).

For these reasons, volume was used to compensate for volume-related uncharacterized factors such as baseline necrotic cell death and changes in vascularity associated with preclinical tumor size. These can influence cell death responses to chemotherapy and often cannot be controlled in a preclinical setting, The results confirmed that the correlation between ΔAAC and CDF indeed improved when ΔAAC was normalized to initial tumor volume (from r^2 of 0.399 to 0.688) and when it was included as an additional biological parameter in the predictive model (r^2 of 0.74).

The reduction in cell size observed histologically and associated with cell death could not be well detected by scatterer property estimates. The ASDs estimated by both models were considerably larger than cells (five times larger at low frequency and two times larger at high frequency). In a tumor study comparing three form factor models for characterizing mammary carcinoma and sarcoma tumors in mouse models, Oelze et al. demonstrated that the SGM best predicted the size of cell scatterers, although the FFSM provided better fits to the backscatter power [28]. In contrast, the high-frequency backscatter data here were fitted better with the SGM model. This suggests that, depending on the tumor type and the ultrasound frequency being used, the SGM model may also describe scattering by an aggregate of cells, rather than individual cells, as was previously hypothesized by Oelze et al. [28].

Analysis of changes in AAC with treatment indicated greater increases in AAC estimated from low-frequency data compared with those estimated from high-frequency data after 24 hours (nearly 2 dB higher). This observation was consistent with previous findings *in vitro*: in the 10- to 30-MHz range, cell samples treated with chemotherapy demonstrated a 5-dB increase in backscatter amplitude, whereas in the 30- to 50-MHz range, a lesser 2-dB increase was observed [42]. The fact that the ANOVA test revealed no statistically significant difference among treatment times at both frequencies is not surprising because of tumor variations in vascularity and baseline necrosis previously explained which affect QUS parameter estimation. Nevertheless, *post hoc* tests revealed statistically significant differences at 24 hours at both frequencies. This was due to the fact that 24 hours is the time required for cytotoxic drugs to induce apoptosis on the tumor (as suggested by the highest CDF measured and as demonstrated in a previous study [43]).

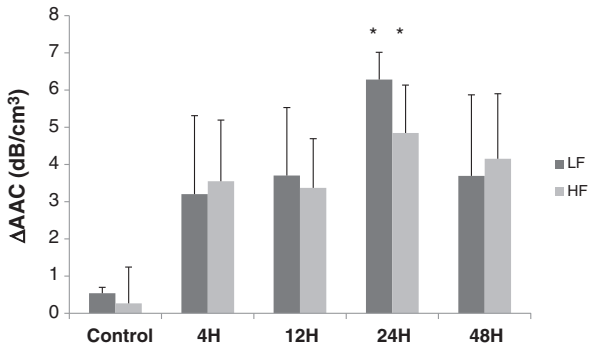

Figure 5. Plot of ΔAAC versus time from treatment onset. Gray bars represent mean low-frequency estimates, and black bars represent mean high-frequency estimates. Error bars represent the standard error across the tumor samples for each time condition. *Statistically significant difference from control ($P < .05$).

Multiple regression analysis of QUS versus CDF demonstrated the "best" single parameter based on the experiments conducted to be ΔAAC and the "best" multiparameter model to be ΔAAC, ΔHI_{ASD}, and V_i. It is believed that ΔHI_{ASD} reflects changes in heterogeneity of the tumor in response to therapy. The improvement obtained by adding V_i to the regression model suggests that initial tumor volume affects the BSC parameters and CDF and is an important parameter. The rationale is that larger tumors often develop necrotic and/or hypoxic regions and also have a differential vascular content which could potentially alter the acoustic scattering properties.

In a recent clinical QUS study which examined changes in AAC and ASD estimated from the FFSM fitting of the BSC from patient breast tumors, significant increases in AAC were observed as early as 1 week after the start of treatment [30]. However, no corresponding histopathological data were available during the treatment to compare AAC changes with microstructural changes in the tumor. Rather, AAC changes measured during the treatment were compared with clinical response determined based on tumor size reduction at the end of the treatment which generally lasts several months. The low- (and clinically relevant) frequency preclinical study performed here, backed by high-frequency data, suggests that the increases in AAC observed clinically during anticancer treatment are likely associated with cell death response. However, the findings of this study suggest that other factors such as tumor heterogeneity and initial tumor volume should also be taken into account when assessing tumor response. Other studies have begun to assess such factors using image-based texture analysis to account for tumor heterogeneity [44]. Other studies have

Table 3B. Stepwise Multiple Regression Results for the Two Cases—with and without Tumor Volume Normalization (Separated by a Horizontal Line)

	Predictive Model Parameter	Standardized Model Coefficient	Correlation to CDF
Without normalization	**Δ**AAC	0.765	0.399
	ΔHI_{ASD}	0.429	0.068
	V_i	0.336	0.197
With normalization	**Δ**AAC_{VN}	0.829	0.688

The second column presents the standardized coefficient of each model parameter, and the third column presents the parameter's correlation to CDF (r^2).

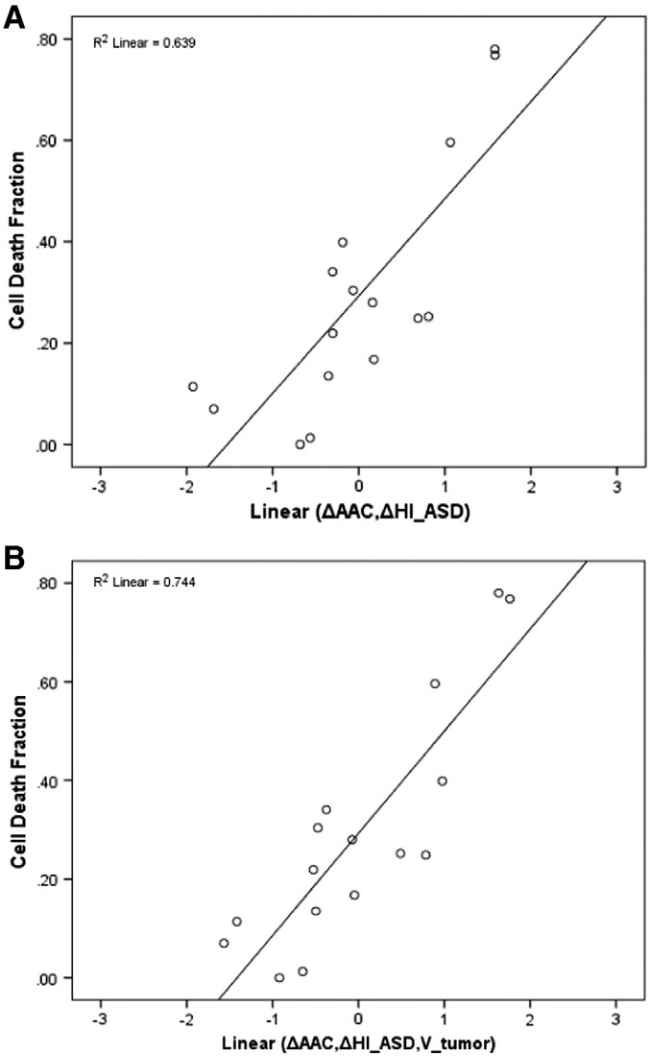

Figure 6. Scatter plots of CDF versus different predictive models with lines of least squares fit (A). Predictive model was the linear combination of AAC and SD(ASD), resulting in $R^2 = 0.639$. (B) Predictive model was the linear combination of AAC, SD(ASD), and V_i, resulting in $R^2 = 0.744$.

demonstrated recently also the effect of tumor vascularity on QUS parameters [45].

The fact that SGM form factor fitted the measured BSC better compared with the FFSM form factor may owe to the theory that the SGM model better reflects the acoustic impedance autocorrelation function of the tumor. As mentioned previously, form factors are proportional to the Fourier transform of the spatial autocorrelation of the relative acoustic impedance between the scatterer and the background. A continuous change in acoustic impedance between the scatterer and its background, which is assumed in the SGM model, may better reflect the interface between tumor cell clusters and the extracellular matrix, as opposed to a discrete change in acoustic impedance described by the FFSM model.

In conclusion, scatterer property-based QUS biomarkers, including ΔAAC, ΔHI_{ASD}, and V_i, demonstrated a favorable correlation to cell death extent (CDF). The results of this work are promising for the development of QUS imaging methods for monitoring of breast tumor response to anticancer therapy, requiring only a standard clinical US scanner equipped with QUS processing and imaging software.

Acknowledgements

H.T. held a Natural Sciences and Engineering Research Council of Canada Alexander Graham Bell Graduate Scholarship. A.S.N. held a Banting Postdoctoral Fellowship and also held a Canadian Breast Cancer Foundation Postdoctoral Fellowship partly during the conduct of this research. M.C.K. holds a Tier 2 Canada Research Chair in Biomedical Applications of Ultrasound. G.J.C. held a Cancer Care Ontario Research Chair in Experimental Therapeutics and Imaging and now holds University of Toronto James and Mary Davie Chair in Breast Cancer Imaging and Ablation. This study was funded, in part, by the Canadian Breast Cancer Foundation, Ontario Region. Funding for this project was also provided by the Terry Fox Foundation, the Natural Sciences and Engineering Research Council of Canada, and the Canadian Institutes of Health Research. The authors disclose no conflict of interest.

References

[1] Eisenhauer EA, Therasse P, Bogaerts J, Schwartz LH, Sargent D, Ford R, Dancey J, Arbuck S, Gwyther S, and Mooney M, et al (2009). New response evaluation criteria in solid tumours: revised RECIST guideline (version 1.1). *Eur J Cancer* **45**(2), 228–247.

[2] Brindle K (2008). New approaches for imaging tumour responses to treatment. *Nat Rev Cancer* **8**(2), 94–107.

[3] Moffat BA, Chenevert TL, Lawrence TS, Meyer CR, Johnson TD, Dong Q, Tsien C, Mukherji S, Quint DJ, and Gebarski SS, et al (2005). Functional diffusion map: a noninvasive MRI biomarker for early stratification of clinical brain tumor response. *Proc Natl Acad Sci U S A* **102**(15), 5524–5529.

[4] Schelling M, Avril N, Nährig J, Kuhn W, Römer W, Sattler D, Werner M, Dose J, Jänicke F, and Graeff H, et al (2000). Positron emission tomography using [(18)F]fluorodeoxyglucose for monitoring primary chemotherapy in breast cancer. *J Clin Oncol Off J Am Soc Clin Oncol* **18**(8), 1689–1695.

[5] Falou O, Soliman H, Sadeghi-Naini A, Iradji S, Lemon-wong S, Zubovits J, Spayne J, Dent R, Trudeau M, and Boileau JF, et al (2012). Diffuse optical spectroscopy evaluation of treatment response in women with locally advanced breast cancer receiving neoadjuvant chemotherapy. *Transl Oncol* **5**(4), 238–246.

[6] D'Astous FT and Foster FS (1986). Frequency dependence of ultrasound attenuation and backscatter in breast tissue. *Ultrasound Med Biol* **12**(10), 795–808.

[7] Tadayyon H, Sadeghi-Naini A, Wirtzfeld L, Wright FC, and Czarnota G (2014). Quantitative ultrasound characterization of locally advanced breast cancer by estimation of its scatterer properties. *Med Phys* **41**(1), 012903.

[8] Tadayyon H, Sadeghi-Naini A, and Czarnota GJ (2014). Noninvasive characterization of locally advanced breast cancer using textural analysis of quantitative ultrasound parametric images. *Transl Oncol* **7**(6), 759–767.

[9] Feleppa EJ, Kalisz A, Sokil-Melgar JB, Lizzi FL, Liu T, Rosado AL, Shao MC, Fair WR, Wang Y, and Cookson MS, et al (1996). Typing of prostate tissue by ultrasonic spectrum analysis. *IEEE Trans Ultrason Ferroelectr Freq Control* **43**(4), 609–619.

[10] Sadeghi-Naini A, Sofroni E, Papanicolau N, Falou O, Sugar L, Morton G, Yaffe MJ, Nam R, Sadeghian A, and Kolios MC, et al (2015). Quantitative ultrasound spectroscopic imaging for characterization of disease extent in prostate cancer patients. *Transl Oncol* **8**(1), 25–34.

[11] Mamou J, Coron A, Oelze ML, Saegusa-Beecroft E, Hata M, Lee P, Machi J, Yanagihara E, Laugier P, and Feleppa EJ (2011). Three-dimensional high-frequency backscatter and envelope quantification of cancerous human lymph nodes. *Ultrasound Med Biol* **37**(3), 345–357.

[12] Fellingham LL and Sommer FG (1984). Ultrasonic characterization of tissue structure in the in vivo human liver and spleen. *IEEE Trans Sonics Ultrason* **SU-31**(4), 418–428.

[13] Suzuki K, Hayashi N, Sasaki Y, Kono M, Kasahara A, Imai Y, Fusamoto H, and Kamada T (1993). Evaluation of structural change in diffuse liver disease with frequency domain analysis of ultrasound. *Hepatology* **17**(6), 1041–1046.

[14] Machado CB, Pereira WCA, Meziri M, and Laugier P (2006). Characterization of in vitro healthy and pathological human liver tissue periodicity using backscattered ultrasound signals. *Ultrasound Med Biol* **32**(5), 649–657.

[15] Abeyratne UR and Tang X (2007). Ultrasound scatter-spacing based diagnosis of focal diseases of the liver. *Biomed Signal Process Control* **2**(1), 9–15.

[16] Bosisio MR, Maisonneuve C, Gregoire S, Kettaneh A, Mueller CG, and Bridal SL (2009). Ultrasound biomicroscopy: a powerful tool probing murine lymph node size in vivo. *Ultrasound Med Biol* **35**(7), 1209–1216.

[17] Miura K, Nasu H, and Yamamoto S (2013). Scanning acoustic microscopy for characterization of neoplastic and inflammatory lesions of lymph nodes. *Sci Rep* **3**, 1255.

[18] Czarnota GJ, Kolios MC, Vaziri H, Benchimol S, Ottensmeyer FP, Sherar MD, and Hunt JW (1997). Ultrasonic biomicroscopy of viable, dead and apoptotic cells. *Ultrasound Med Biol* **23**(6), 961–965.

[19] Czarnota GJ, Kolios MC, Abraham J, Portnoy M, Ottensmeyer FP, Hunt JW, and Sherar MD (1999). Ultrasound imaging of apoptosis: high-resolution noninvasive monitoring of programmed cell death in vitro, in situ and in vivo. *Br J Cancer* **819**(3), 520–527.

[20] Brand S, Weiss EC, Lemor RM, and Kolios MC (2008). High frequency ultrasound tissue characterization and acoustic microscopy of intracellular changes. *Ultrasound Med Biol* **34**(9), 1396–1407.

[21] Banihashemi B, Vlad R, Debeljevic B, Giles A, Kolios MC, and Czarnota GJ (2008). Ultrasound imaging of apoptosis in tumor response: novel preclinical monitoring of photodynamic therapy effects. *Cancer Res* **68**(20), 8590–8596.

[22] Vlad RM, Brand S, Giles A, Kolios MC, and Czarnota GJ (2009). Quantitative ultrasound characterization of responses to radiotherapy in cancer mouse models. *Clin Cancer Res Off J Am Assoc Cancer Res* **15**(6), 2067–2075.

[23] Sadeghi-Naini A, Falou O, Tadayyon H, Al-Mahrouki A, Tran W, Papanicolau N, Kolios MC, and Czarnota GJ (2013). Conventional Frequency Ultrasonic Biomarkers of Cancer Treatment Response In Vivo. *Transl Oncol* **6**(3), 234–243.

[24] Lizzi FL, King DL, Rorke MC, Hui J, Ostromogilsky M, Yaremko MM, Feleppa EJ, and Wai P (1988). Comparison of theoretical scattering results and ultrasonic data from clinical liver examinations. *Ultrasound Med Biol* **14**(5), 377–385.

[25] Silverman RH, Folberg R, Rondeau MJ, Boldt HC, Lloyd HO, Chen X, Lizzi FL, Weingeist TA, and Coleman DJ (2003). Spectral parameter imaging for detection of prognostically significant histologic features in uveal melanoma. *Ultrasound Med Biol* **29**(7), 951–959.

[26] Lizzi FL, Ostromogilsky M, Feleppa EJ, Rorke MC, and Yaremko MM (1986). Relationship of ultrasonic spectral parameters to features of tissue microstructure. *IEEE Trans Ultrason Ferroelectr Freq Control* **UFFC-33**(3), 319–329.

[27] Insana MF and Hall TJ (1990). Parametric ultrasound imaging from backscatter coefficient measurements: image formation and interpretation. *Ultrason Imaging* **12**(4), 245–267.

[28] Oelze ML and O'Brien WD (2006). Application of three scattering models to characterization of solid tumors in mice. *Ultrason Imaging* **28**(2), 83–96.

[29] Oelze ML, O'Brien Jr WD, Blue JP, and Zachary JF (2004). Differentiation and Characterization of Rat Mammary Fibroadenomas and 4T1 Mouse Carcinomas Using Quantitative Ultrasound Imaging. *IEEE Trans Med Imaging* **23**(6), 764–771.

[30] Sannachi L, Tadayyon H, Sadeghi-Naini A, Tran W, Gandhi S, Wright F, Oelze M, and Czarnota G (2014). Non-invasive evaluation of breast cancer response to chemotherapy using quantitative ultrasonic backscatter parameters. *Med Image Anal* **20**(1), 224–236.

[31] Insana MF, Wagner RF, Brown DG, and Hall TJ (1990). Describing small-scale structure in random media using pulse-echo ultrasound. *J Acoust Soc Am* **87**(1), 179–192.

[32] Taggart LR, Baddour RE, Giles A, Czarnota GJ, and Kolios MC (2007). Ultrasonic characterization of whole cells and isolated nuclei. *Ultrasound Med Biol* **33**(3), 389–401.

[33] Czarnota GJ and Kolios MC (2001). Ultrasound imaging of apoptosis: role of chromatin structure and membrane configuration. Proc Am Inst Ultra Med Annu Meeting; 2001. p. 117.

[34] Sadeghi-Naini A, Papanicolau N, Falou O, Tadayyon H, Lee J, Zubovits J, Sadeghian A, Karshafian R, Al-Mahrouki A, and Giles A, et al (2013). Low-frequency quantitative ultrasound imaging of cell death in vivo. *Med Phys* **40**(8), 082901.

[35] Topp KA, Zachary JF, and O'Brien Jr WD (2001). Quantifying B-mode images of in vivo rat mammary tumors by the frequency dependence of backscatter. *J Ultrasound Med* **20**(6), 605–612.

[36] Yao LX, Zagzebski JA, and Madsen EL (1990). Backscatter coefficient measurements using a reference phantom to extract depth-dependent instrumentation factors. *Ultrason Imaging* **12**(1), 58–70.

[37] Madsen EL, Zagzebski JA, Banjavie RA, and Jutila RE (1978). Tissue mimicking materials for ultrasound phantoms. *Med Phys* **5**(5), 391–394.

[38] Shung K (2005). Diagnostic ultrasound: imaging and blood flow measurements. CRC Press; 2005 .

[39] Nam K, Zagzebski JA, and Hall TJ (2013). Quantitative assessment of in vivo breast masses using ultrasound attenuation and backscatter. *Ultrason Imaging* **35**(2), 146–161.

[40] Partridge SC, Gibbs JE, Lu Y, Esserman LJ, Tripathy D, Wolverton DS, Rugo HS, Hwang ES, Ewing CA, and Hylton NM (2005). MRI measurements of breast tumor volume predict response to neoadjuvant chemotherapy and recurrence-free survival. *AJR Am J Roentgenol* **184**(6), 1774–1781.

[41] Smith IC, Heys SD, Hutcheon AW, Miller ID, Payne S, Gilbert FJ, Ah-See AK, Eremin O, Walker LG, and Sarkar TK, et al (2002). Neoadjuvant chemotherapy in breast cancer: significantly enhanced response with docetaxel. *J Clin Oncol Off J Am Soc Clin Oncol* **20**(6), 1456–1466.

[42] Brand S, Solanki B, Foster DB, Czarnota GJ, and Kolios MC (2009). Monitoring of cell death in epithelial cells using high frequency ultrasound spectroscopy. *Ultrasound Med Biol* **35**(3), 482–493.

[43] Ellis P, Smith I, McCarthy K, Detre S, Salter J, and Dowsett M (1997). Preoperative chemotherapy induces apoptosis in early breast cancer. *Lancet* **349**(9055), 849.

[44] Sadeghi-Naini A, Sannachi L, Pritchard K, Trudeau M, Gandhi S, Wright FC, Zubovits J, Yaffe MJ, Kolios MC, and Czarnota GJ (2014). Early prediction of therapy responses and outcomes in breast cancer patients using quantitative ultrasound spectral texture. *Oncotarget* **5**(11), 3497–3511.

[45] Kaffas AE, Sadeghi-Naini A, Falou O, Tran WT, Zhou S, Hashim A, Fernandes J, Giles A, and Czarnota GJ (2015). Assessment of tumor response to radiation and vascular targeting therapy in mice using quantitative ultrasound spectroscopy. *Med Phys* **42**(8), 4965–4973.